Atmospheric Research 92 (2009) 190–211

Contents lists available at ScienceDirect

Atmospheric Research

journal homepage: www.elsevier.com/locate/atmos

Improving the behavior of the cumulus parameterization for tropical cyclone prediction: Convection trigger

Lei-Ming Ma [a,b,*], Zhe-Min Tan [a]

[a] Key Laboratory of Mesoscale Severe Weather/MOE, and Department of Atmospheric Sciences, Nanjing University, Nanjing 210093, PR China
[b] Laboratory of Typhoon Forecast Technique/CMA, Shanghai Typhoon Institute, Shanghai 200030, PR China

ARTICLE INFO

Article history:
Received 18 March 2008
Received in revised form 26 August 2008
Accepted 24 September 2008

Keywords:
Cumulus parameterization
Tropical cyclone
Numerical simulation

ABSTRACT

Numerical studies have consistently shown the importance of moist convection in the evolution of tropical cyclones. However, a systematic evaluation of cumulus parameterization in the simulation of tropical cyclone is rare. The objective of this study is to 1) assess the performance of various subgrid-scale cumulus parameterization schemes in the simulation of tropical cyclones. Emphasis is placed on the intensity, distribution, and character of precipitation and on the forecast location and intensity of tropical cyclones; 2) improve the behavior of one of the cumulus parameterization schemes by modifying the parameterization, the weakness of which is identified in 1).

The distribution and intensity of precipitation, its partitioning into grid-resolvable and subgrid-scale portions, the location and intensity of tropical cyclone were extremely sensitive to the choice of cumulus parameterization scheme. The scheme developed by Betts and Miller [Betts, A.K., Miller, M.J., 1993. The Betts–Miller scheme. In:Emanuel, K.A., Raymond, D.J. (Eds.), The Representation of Cumulus Convection in Numerical Models. Amer. Meteor. Soc., 246 pp] reproduced most of the features of rainfall distribution over the land, it tends to overestimate the rainfall coverage and make false alarm of intense rainfall. The mass flux scheme developed by Kain and Fritsch [Kain, J.S., Fritsch, J.M., 1993. Convective parameterization for mesoscale models: the Kain–Fritsch scheme. The Representation of Cumulus Convection in Numerical Models, Meteor. Monogr., No. 46, Amer. Meteor. Soc., 165–170] gave the best simulation of tropical cyclone on the 15 km grids, while the quasi-equilibrium scheme proposed by Grell [Grell, G., 1993. Prognostic evaluation of assumptions used by cumulus parameterization. Mon. Weather Rev., 121, 764–787] tended to underestimate sub-grid scale rainfall due to its deficiency in removing instability. Finally, it is also suggested that the Kain–Fritsch scheme can be improved for the case of weak synoptic forcing. In particular, the parameterization of the convective parcel's temperature perturbation by the environmental vertical velocity in the convective trigger function seems not quite robust. To improve this deficiency for our application, the effect of moisture advection is taken into account in determining the convective parcel's temperature perturbation. Preliminary results show that, the modified scheme can eliminate reasonably well the convective instability under weak synoptic forcing, change the response of the disturbance in the lower troposphere disturbance to environmental humidity and in favor of simulation of tropical cyclone. The results of this study should be of potential use for improving the performance of operational tropical cyclone prediction.

* Corresponding author. Laboratory of Typhoon Forecast Technique/CMA, Shanghai Typhoon Institute, Shanghai 200030, PR China.
E-mail address: malm@mail.typhoon.gov.cn (L.-M. Ma).

0169-8095/$ – see front matter © 2008 Elsevier B.V. All rights reserved.
doi:10.1016/j.atmosres.2008.09.022

1. Introduction

The concept of cumulus parameterization (hereafter CP) was proposed by Charney and Eliassen (1964) and Ooyama (1964) in tropical cyclone (hereafter TC) modeling. By formulating the collective effects of moist convection in terms of the model explicit processes, the objective of CP is to represent the effect of an ensemble of cumulus clouds on the large scale flow and to obtain a closed system for numerical prediction (Arakawa, 2004). A number of CP schemes have been developed over the years (e.g., Ooyama, 1971; Kuo, 1974; Arakawa and Schubert, 1974; Fritsch and Chappel, 1980; Betts, 1986; Frank and Cohen, 1987; Tiedtke, 1989; Emanuel, 1991; Grell, 1993; Kain and Fritsch, 1990, 1993; Kain, 2004), most of which have been successfully implemented in research and operational applications (Wang and Seaman, 1997; Kuo et al., 1996, 1997).

Despite these efforts, CP is still an unsolved scientific problem (Arakawa, 2004) because of the uncertain basis of its theory. For instance, Ooyama (1964) emphasized the importance of surface friction in producing low-level convergence in the genesis of convective clouds. However, Ceselski (1974) pointed out that frictional pumping is neither a necessary nor a sufficient cause for the occurrence of cumulus convection. Controversy between the theory of conditional instability of the second kind (CISK) and wind-induced surface heat exchange (WISHE, Emanuel, 1986) has made the concept of CP questionable.

In an effort to avoid these controversies, explicit cloud models have been developed as computational power continues to increase (Zhu and Zhang, 2006; Nasuno et al., 2007). Nevertheless, given the limit of predictability of cloud-scale motions and the difficulties in initialization of cloud models, the simulated convective features usually degrade progressively as resolution is increased, implying that parameterization of unresolved processes may still be necessary and appropriate (Weisman et al., 1997).

Actually, CP schemes are generally implemented in current operational tropical cyclone numerical models, which still have not reached a high enough resolution to run with explicit clouds only. Unfortunately, we still have limited understanding of how to effectively use CP in numerical prediction of TCs. For instance, Puri and Miller (1990) compared the performance of the Kuo and Betts–Miller (1993) schemes using Australian Monsoon Experiment datasets of four TCs and found that vertical consistency of meteorological parameters is better predicted with the Betts–Miller scheme. However, Alapaty et al. (1994) found that TC rainfall is predicted better by the Kuo scheme than by the Betts–Miller scheme with almost similar model parameters as Puri and Miller (1990). These inconsistent results imply that further studies are required to understand the performance of CPs in TC simulations. The trigger function in the CP should perhaps be the first issue examined, for its important role in convection initiation.

In this regard, the objective of this study is to evaluate and enhance the behavior of CPs in numerical prediction of TCs. The paper is organized in five sections. Section 2 describes the methodology of CPs and the vortex initialization technique. Section 3 evaluates the performance of various CPs in TC numerical prediction. Section 4 attempts to improve the algorithm of CP with emphasis on its trigger function. Section 5 is the summary.

2. Methodology

2.1. The concept of CP

CP is a closure problem in which we seek a limited number of equations that govern the statistics of a system with huge dimensions. The area-averaged time rate of change of mean temperature (Anthes, 1977) can be written as

$$\frac{\partial \overline{T}}{\partial t} + \nabla \cdot \overline{V}\overline{T} + \frac{\partial \overline{\omega}\overline{T}}{\partial p} - \frac{\overline{\omega} R \overline{T}}{c_p p} = \frac{L}{c_p}\overline{C^*} - \frac{A\overline{\omega' T'}}{Ap} + \frac{R\overline{\omega' T'}}{c_p p} \quad (1)$$

where C^* is the local condensation or evaporation rate, and the overbar and prime indicate the mean and eddy components, respectively. The terms on the right-hand side of Eq. (1) are the latent heat release in the clouds and the eddy flux of sensible heat. These terms together define the mean temperature change produced by convection, e.g.

$$\frac{\partial \overline{T}}{\partial t}|_{\text{conv}} = \frac{L}{c_p}\overline{C^*} - \frac{A\overline{\omega' T'}}{Ap} + \frac{R\overline{\omega' T'}}{c_p p}. \quad (2)$$

For a CP scheme, a grid-resolved quantity in the numerical model is usually selected to control the amount of convection, while a cloud model is used to estimate the vertical structure of the cloud.

In this study, three CP schemes, the Betts–Miller scheme (Betts and Miller, 1993, hereafter BM93), the Grell scheme (Grell, 1993, hereafter GR93), and the Kain–Fritsch scheme (Kain and Fritsch, 1993, hereafter KF93) are selected for their widespread and successful application.

The BM93 scheme is a lagged convective adjustment scheme proposed by Betts (1986), in which the thermodynamic profile is adjusted toward an observed quasi-equilibrium state as a reference profile. Effects of convective downdrafts are also considered in BM93.

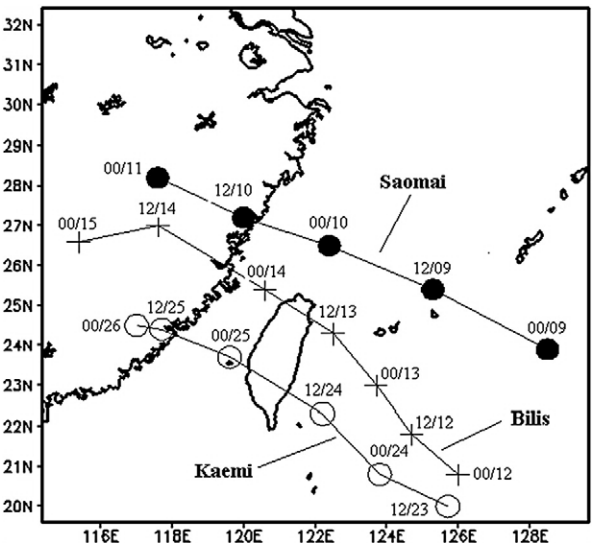

Fig. 1. Tracks for TC Kaemi, Bilis and Saomai in 2006 provided by JTWC. Times with legend hh/dd (hour UTC/day of month) are indicated besides the track.

Table 1
Simulation phases for each of the TC cases

TC name	Bilis	Saomai	Kaemi
Simulation phases (hour UTC/day of month)	00/12–00/13, 12/12–12/13, 00/13–00/14, 12/13–12/14, 00/14–00/15, July, 2006	00/09–00/10, 12/09–12/10, 00/10–00/11, Aug, 2006	12/23–12/24, 00/24–00/25, 12/24–12/25, 00/25–00/26, July, 2006

The GR93 scheme was originally a simple single-cloud version of the Arakawa–Schubert scheme (1974) with parameterized updraft/downdraft fluxes and compensating motion determining the heating/moistening profile. The closure used by the GR93 scheme is the quasi-equilibrium assumption (Arakawa and Schubert, 1974).

The KF93 scheme was originally derived from the Fritsch–Chappell scheme (Fritsch and Chappel, 1980), which employs the Lagrangian parcel method (Simpson and Wiggert, 1969), and vertical momentum dynamics (Donner, 1993), to estimate whether instability exists, whether any existing instability will become available for cloud growth, and what the properties of convective clouds might be. It is convenient to divide the KF scheme into three parts: 1) convection trigger, 2) mass fluzx algorithm, and 3) closure assumptions. The closure assumption in the KF parameterization is the same as that used in the Fritsch–Chappell scheme, in which once convection is triggered, CAPE is assumed to be removed in a grid column within an advective time period (Kain and Fritsch, 1993). The KF93 scheme utilizes a mass-conservative cloud model, which includes parameterized moist downdrafts, entrainment and detrainment at the cloud edge (Kain and Fritsch, 1990) and allows interaction between cloud and environment. In addition to the CPs, an explicit prediction scheme for rainwater and cloud water with simple ice physics (Dudhia, 1989) is employed.

2.2. Numerical model

We performed numerical simulations with the nonhydrostatic version of the PSU-NCAR Mesoscale Model version 5 (MM5; Grell et al., 1994). The application of the MM5 model has been successful in simulating convective systems in tropical and subtropical regions. In particular, it has been successfully used to reproduce the structure and changes in intensity of TCs over the oceans (Liu et al., 1997). In our MM5 simulations, the initial fields and lateral boundary conditions are derived from the NCEP/GFS Model, the horizontal resolution of which is 1°×1°. The initial fields are interpolated onto a single computational domain with mesh size of 118×118 grid points at resolution of 15 km. This resolution is set to be consistent with the assumptions of the above CP schemes. 28 vertical

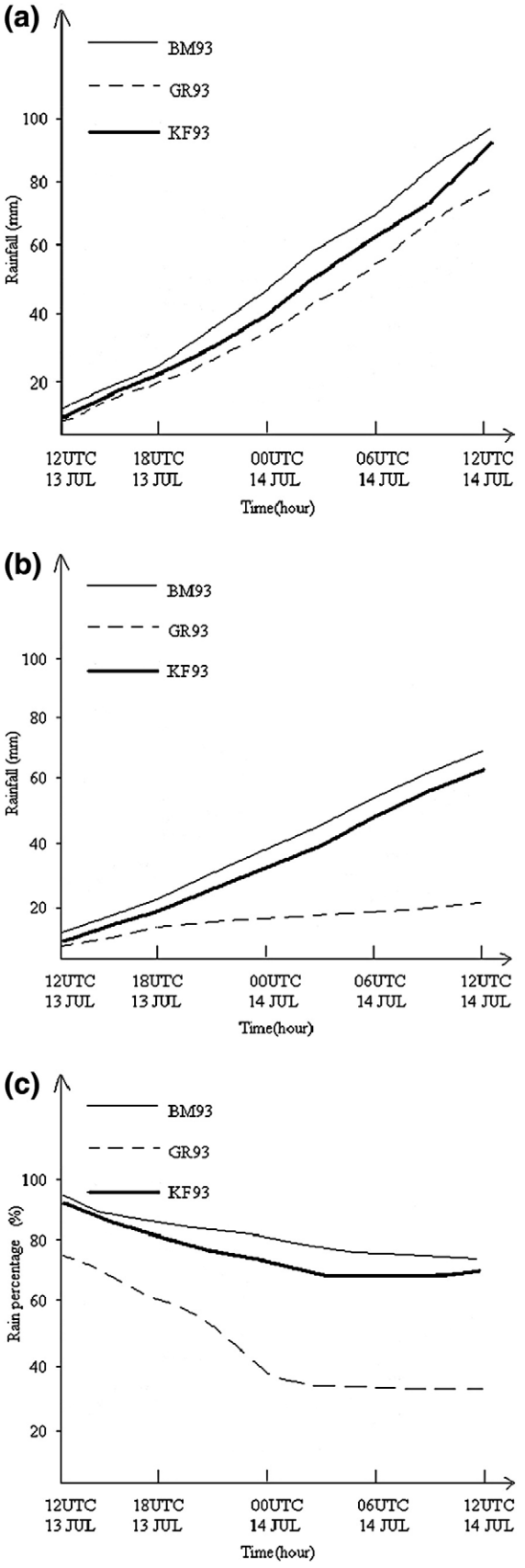

Fig. 2. Temporal evolution of the domain-averaged (a) total surface rainfall accumulation (mm), (b) subgrid surface rainfall accumulation (mm), and (c) percentage of the total rainfall that is attributed to subgrid processes for Bilis during 1200 UTC 13 July–1200 UTC 14 July, 2006 with the BM93, GR93 and KF93.

sigma levels (1.00, 0.99, 0.98, 0.96, 0.94, 0.91, 0.88, 0.84, 0.80, 0.75, 0.70, 0.65, 0.61, 0.57, 0.54, 0.51, 0.48, 0.45, 0.42, 0.38, 0.34, 0.30, 0.25, 0.20, 0.15, 0.10, 0.06, and 0.00) were used. The pressure at the top of the model is 50 hPa. Notice that there is a well-resolved planetary boundary layer (PBL) located below the 850-mb level. PBL processes are treated using the scheme of Hong and Pan (1996) due to its capability for simulating the structure and diurnal variability of the boundary layer over land and ocean.

2.3. Vortex initialization with bogus data assimilation

A bogus data assimilation (BDA) scheme (Zou and Xiao, 2000; Xiao et al., 2000), which has been verified in simulations

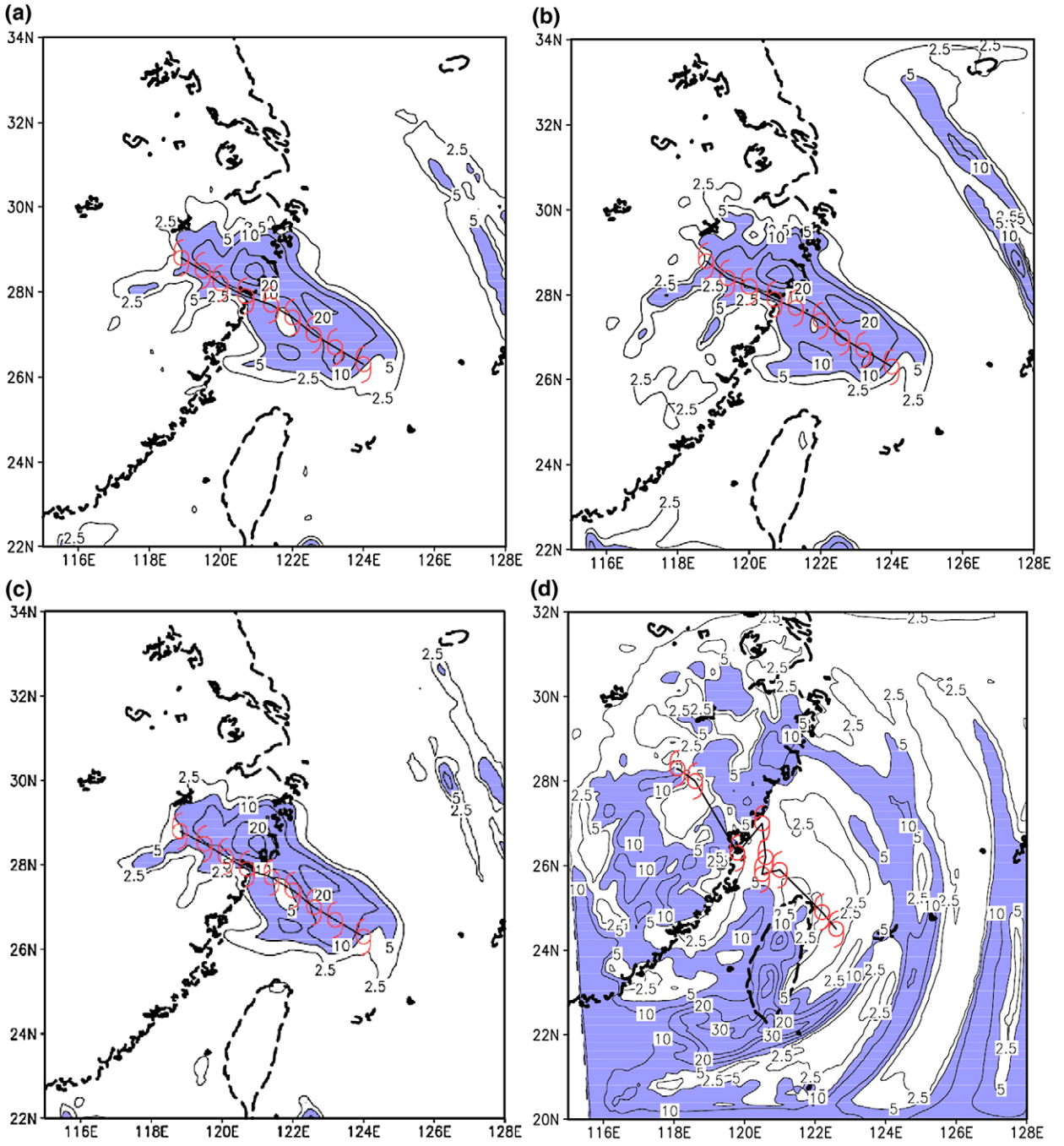

Fig. 3. 24 h-accumulated total rainfall for Saomai during 1200 UTC 9–1200 UTC 10 Aug. 2006 (a—BM93, b—GR93, c—KF93, g—TRMM/TMI 3B42 observation) and Bilis (d—BM93, e—GR93, f—KF93, h—TRMM/TMI 3B42 observation) during 1200 UTC 13–1200 UTC 14 Jul. 2006. The shaded area shows the region with rainfall accumulation exceeding 5 mm/24 h.

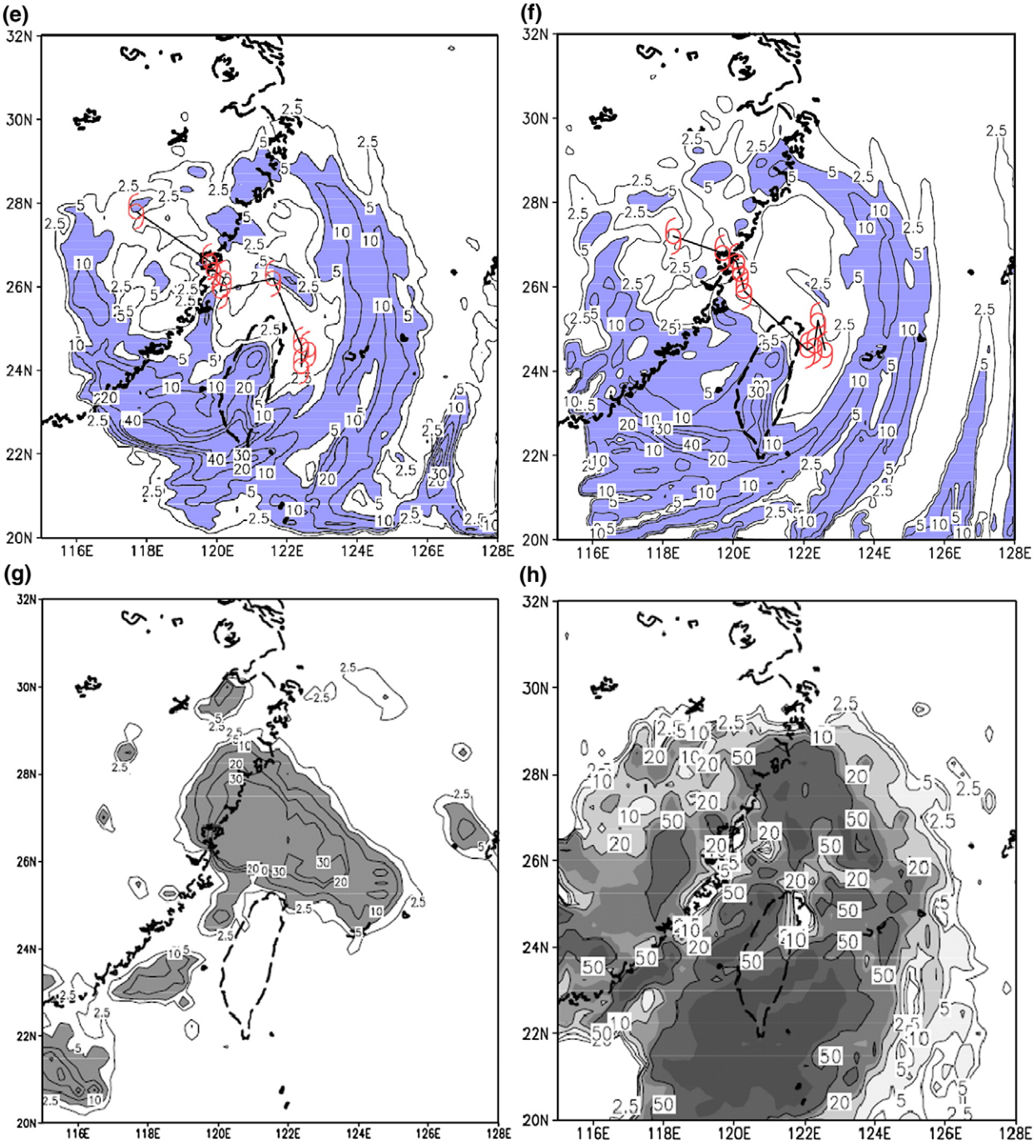

Fig. 3 (*continued*).

of TC Danas (2001) (Ma et al., 2006), is introduced in this study to generate a reasonable TC vortex at the initial time. The BDA scheme consists of two steps: 1) specification of a bogus sea level pressure (SLP) field based on observed TC parameters given by the China Meteorological Administration (CMA); 2) assimilation of the bogus SLP field into the forecast model. Specification of the bogus SLP was based on Fujita's formula with the estimated central SLP pressure and the radius of the outermost closed isobar as inputs. The PSU-NCAR nonhydrostatic adjoint modeling system (Zou et al., 1997) is used for the data assimilation. Within the BDA a dynamically and physically consistent initial condition for the TC can be reached by fitting the forecast model to a specified bogus surface low. Although the BDA has a tendency to spin down in the early

Table 2
Case-averaged Threat Scores (TS) and Bias for 24-h simulation of rainfall accumulation

Thresholds (mm/24 h)	KF93		BM93		GR93	
	TS	Bias	TS	Bias	TS	Bias
0.1	0.231	1.715	0.245	1.455	0.212	0.851
10.0	0.065	1.547	0.072	1.326	0.033	0.784
25.0	0.006	1.231	0.004	1.768	0.002	0.730

model hours (i.e. 0–6 h), it is recognized in this study that the BDA scheme can produce a somewhat realistic TC structure in which most of the sophisticated convective processes are active and contribute to a realistic simulation of rainfall (discuss later).

3. Behavior of cumulus schemes in TC simulations

3.1. Case description and experiment design

The performance of the CPs has been evaluated in both short-term forecast mode (Wang and Seaman, 1997; Kuo et al., 1997; Yang and Tung, 2003; Ma et al., 2004; Mapes, 2004; Hogan and Pauley, 2007), and longer forced runs (Gochis et al., 2002). However, results are difficult to summarize, since the performance of CPs may be sensitive to region, season, synoptic type and forecast range. To evaluate the three cumulus parameterization schemes, three special TC cases are chosen (Fig. 1), which made landfall on China's eastern coast in 2006. 1) Bilis, the most destructive TC to make landfall in China in the last 50 years; 2) Saomai, which underwent unexpected intensification during landfall; and 3) Kaemi, for which the operational forecast failed to predict its slow westward motion after landfall.

The rainfall datasets used for verification include TRMM/TMI retrieved rainfall rates (Kummerow et al., 1998; Ma et al., 2007) and accumulated rainfall observed by the Chinese network of automatic weather stations (Li et al., 2008). The TC track datasets were provided by the Joint Typhoon Warning Center (JTWC) of the USA.

TC Bilis originated as a depression in the northwest Pacific on 8 July and reached tropical storm intensity the following day. Bilis made its first landfall over Taiwan, traversed the Taiwan Straight and eventually landed in Fujian Province. Bilis's movement was normal over the sea. What was unusual was that, despite being degraded to a tropical depression after landing, Bilis continued to move north at a very slow speed from 14 to 18 July, under the influence of the continental high to the north, with its impacts extending for up to five days. Bilis caused widespread flooding and landslides as it moved inland, killing at least 228 people, cause economic losses of around 12 bn yuan (US $1.5 bn).

TC Saomai developed in the western Pacific Ocean on 4 August, passed through Guam on 5 August as a tropical storm. It reached typhoon status the following day and hit the Chinese coastline on 10 July, just south of Wenzhou City. The sustained maximum wind was around 68 m s^{-1} at the time of landfall. Saomai was a TC that strengthened suddenly, and became one of the strongest TCs that ever occurred over China's coastal region.

TC Kaemi emerged over the north-west Pacific Ocean on 18 July and strengthened into a typhoon two days later. Kaemi hit south-western Taiwan on 24 July with maximum sustained winds of 40 m s^{-1}. After moving through Taiwan, Kaemi continued its north-westerly track and came ashore as a tropical storm near Jinjiang City of Fujian Province on 25 July, dumping heavy rainfall in the region. Unfortunately, most of the operational TC forecasts failed to predict its westward track after landfall.

A total of 36 24-hour numerical simulations were conducted for each of the 12 temporal phases (Table 1) to evaluate the performance of BM93, GR93, and KF93. Except for the different options of the CP, identical initialization methods and physics options were used for each of the simulations.

3.2. Evaluation of results

3.2.1. Rainfall

A statistical summary of the partitioning of precipitation into convective and non-convective types from BM93, GR93 and KF93 in the simulation of TC Bilis during 1200 UTC 13 July–1200 UTC 14 July, 2006 is shown in Fig. 2. It illustrates the temporal evolution of domain-averaged surface rainfall accumulation (Fig. 2a), subgrid surface rainfall accumulation (Fig. 2b), and percentage of the rainfall that is attributed to subgrid scale processes (Fig. 2c). For the rainfall accumulation including subgrid scale and grid scale components, it is found that BM93 produced the highest amount, while the GR93 the least (Fig. 2a). KF93 yields close to the average amount from BM93 and GR93. BM93 and KF93 produce almost identical percentages of subgrid rainfall, both of which start with mainly the subgrid component (more than 90%). This percentage decreases gradually, with the minimum value (70%) at the end of 24 h integration (Fig. 2c). Meanwhile, the GR93 scheme yields the least percentage of subgrid rainfall throughout the simulations. It starts with 74% and ends with 30%. The biggest departure (nearly 50%) for subgrid rainfall percentage between GR93 and BM93 (KF93) appears at the end of integration.

This study verifies the effect of the GR scheme on rainfall simulations, which has raised controversy (e.g., Mapes, 2004; Wang and Seaman, 1997). For example, Mapes (2004)

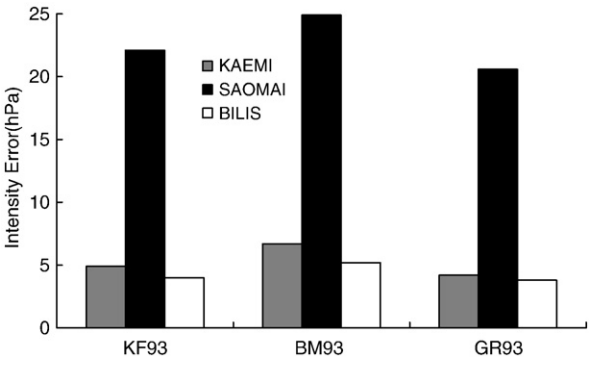

Fig. 4. Case-averaged intensity forecasting error (hPa/24 h) for the different CPS experiments (KF93, BM93, and GR93). Positive values indicate that the intensity is underestimated by models on average.

compared several other CPs in regional simulations of strong mesoscale convective system during the GATE experiment of 1974. They found that the GR93 scheme can be difficult to trigger, frequently yielding little or no rain. However, Wang and Seaman (1997) showed that the GR93 scheme overestimated the areal coverage of convective rainfall while

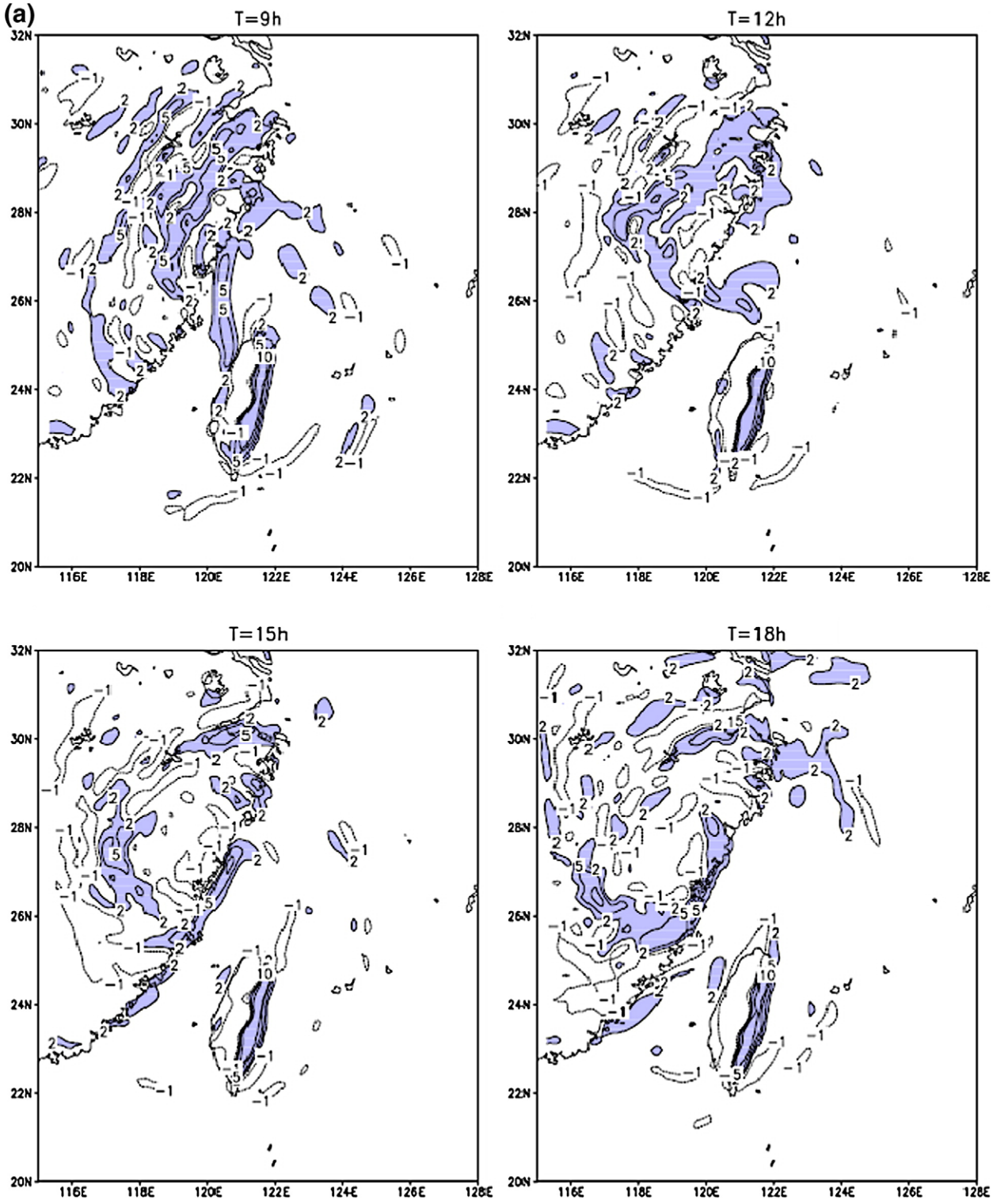

Fig. 5. Potential vorticity (shading at 2 PVU) at 850 hPa produced by experiments. (a) BM93, (b) GR93, and (c) KF93 in simulation of TC Bilis during 21 UTC 13 Jul.–06 UTC 14 Jul. 2006, at 3-h intervals.

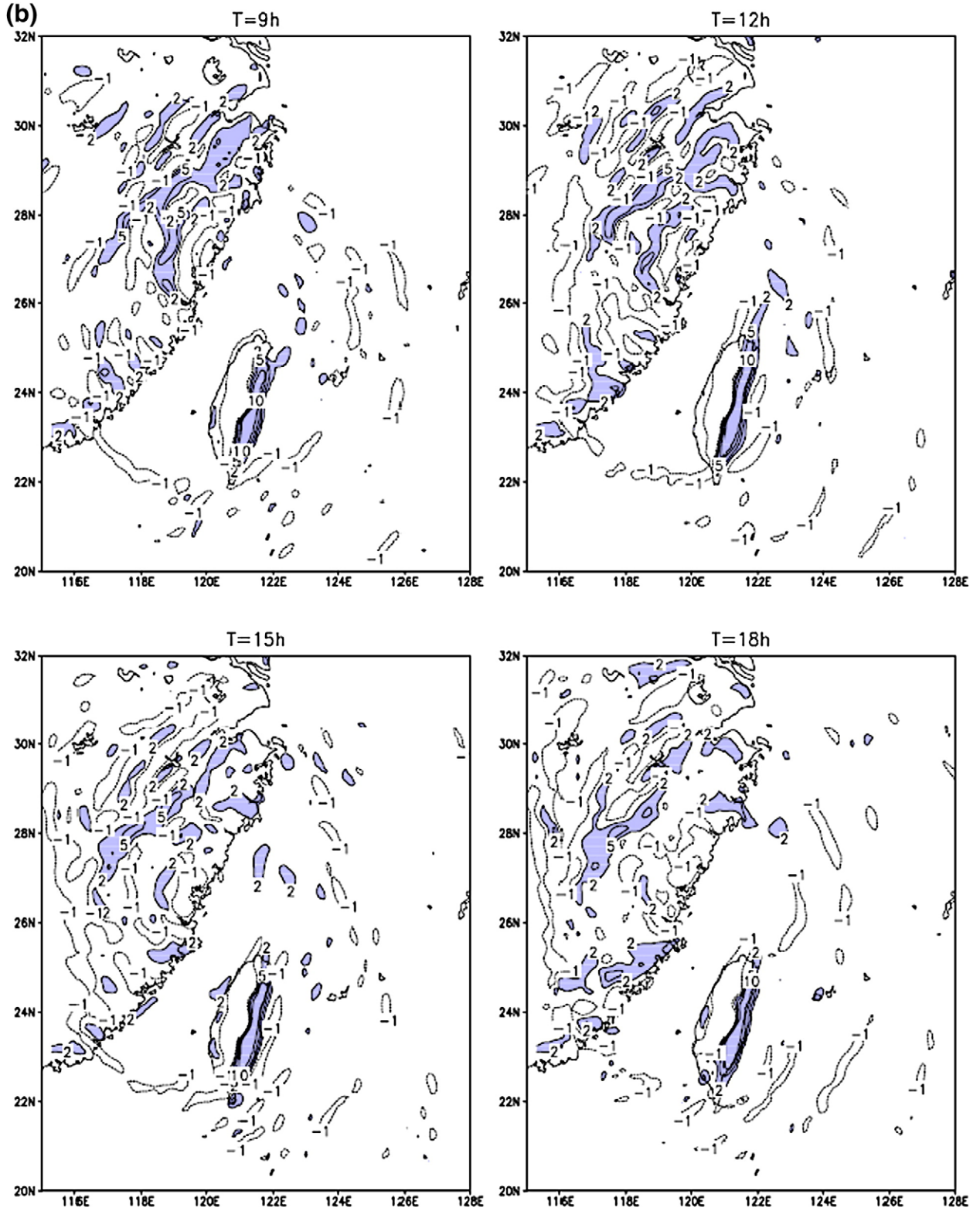

Fig. 5 (*continued*).

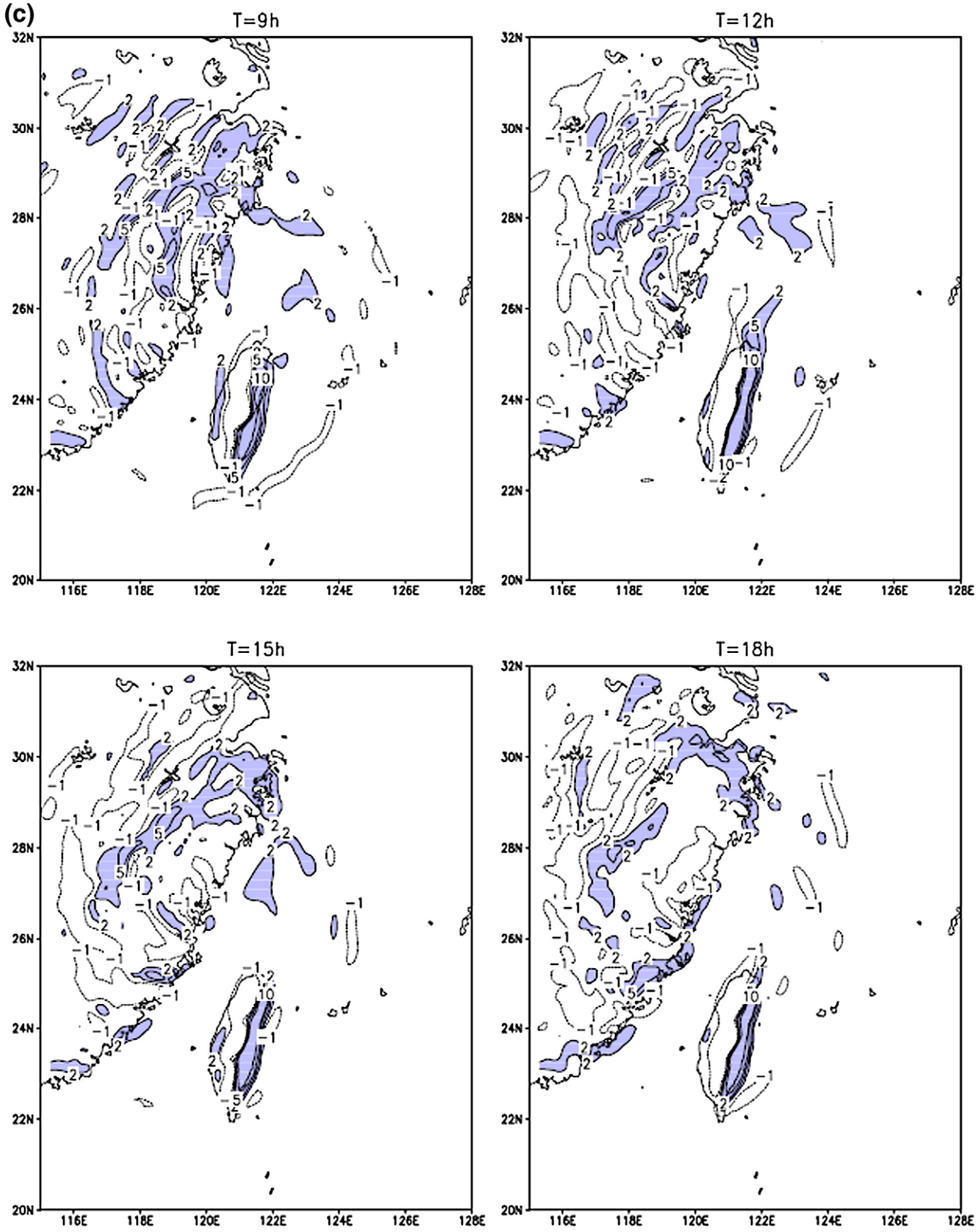

Fig. 5 (*continued*).

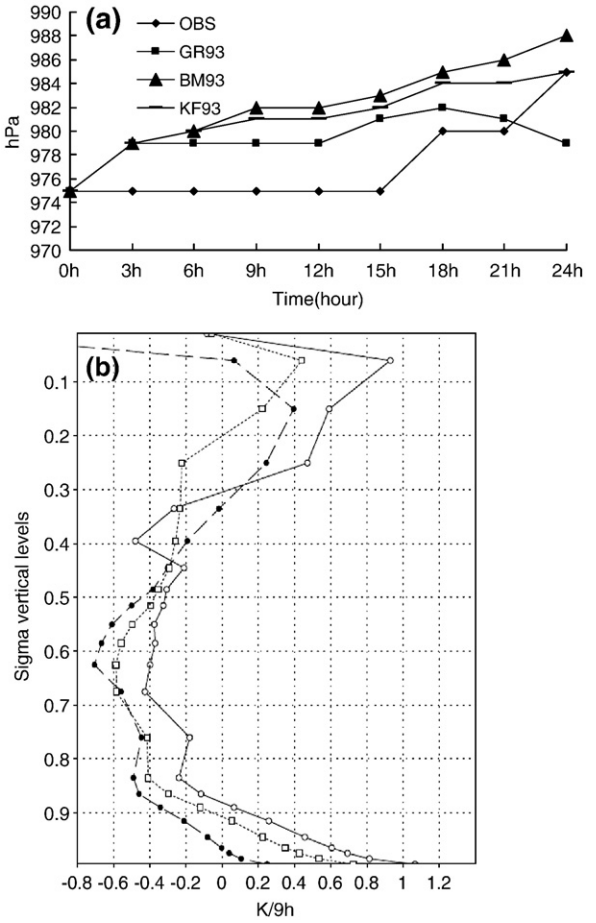

Fig. 6. (a) The temporal evolution of minimum sea level pressure from JTWC analysis (OBS) and three experiments during 12 UTC 13 Jul.–12 UTC 14 Jul. 2006. (b) Domain-averaged vertical heating/cooling profiles (BM93—solid line, GR93—dot line, KF93—long dash line) during 21 UTC 13 Jul.–06 UTC 14 Jul. 2006 from three experiments.

resulting in excessive and localized mesoscale perturbations in precipitation. In this study, it is indicated that the GR93 scheme has a significant tendency to underestimate convective rainfall (Fig. 2b and c), which agrees well with the results of Mapes (2004). This study attributes this low percentage of subgrid rainfall to GR93's inefficiency in removing CAPE in convective unstable situations. For example, during the hour of simulated intense convection (with the subgrid rainfall rate generated by KF93 greater than 10 mm h^{-1}), GR93 reduces the CAPE from 1103 J kg^{-1} to 950 J kg^{-1}, the change of which is less than that of KF93 and BM93, where KF93 reduces the CAPE from 1103 J kg^{-1} to 916 J kg^{-1}, and BM93 from 1103 J kg^{-1} to 920 J kg^{-1}. The GR scheme's underestimation of subgrid scale rainfall is also identified in the simulation of Kaemi (figure is not given).

As a small track error may produce large differences in the geometric patterns of rainfall intensity, evaluation of the 24-h accumulated rainfall is more relevant than temporal evolution of rainfall simulations. Fig. 3 shows that the performance of each CP has a fairly large case-to-case variation in the 24-h accumulated rainfall for various TC events. For example, the simulated 24-h accumulated rainfall during landfall of Saomai, which has a compact structure, shows less sensitivity to various CP schemes than that of Bilis (Fig. 3). While in the case of Bilis, BM93, which generated the broadest area of rainfall, was very different from the rainfalls obtained from KF93 and GR93. Although BM93 reproduced most of the features of rainfall distribution over the land, it tends to overestimate the rainfall coverage and make false alarm of intense rainfall. Table 2 gives the case-averaged Threat Scores (TS) and Bias for 24-h simulation of rainfall accumulation. It is noticed that while the KF93 scheme gives the best TS (0.006) and Bias (1.231) score of heavy rainfall (exceeding 25.0 mm/24 h), the BM93 scheme performs the best in simulating medium (10.0 mm/24 h) to light (0.1 mm/24 h) rainfall.

Although the KF93 scheme tends to overestimate the coverage of light rainfall (0.1 mm/24 h) with the Bias score of 1.715, it appears to be the most robust in that it showed no signs of serious systematic failure on skill measures of medium (10.0 mm/24 h) to heavy rainfall (25.0 mm/24 h).

From idealized sea-breeze simulations with four CPs, Cohen (2002) also made the most realistic rainfall simulation by using Kain–Fritsch scheme, in comparison with those of Betts–Miller scheme and Grell scheme. Meanwhile, Cohen (2002) pointed out the advantage of KF scheme in this case may not be true for other types of convective events. For example, Nagarajan et al. (2001) found it necessary to tune the Kain–Fritsch scheme for a maritime tropical system.

3.2.2. Intensity and Track

For TC intensity, all of the experiments yielded weaker storms than was estimated by JTWC. Intensity errors in minimum sea level pressure ranged from 9.5–14.1 hPa. On average, the GR93 scheme generated the most intensive TC for all the cases, even though it failed to reproduce the intensity of TC Saomai (Fig. 4). In comparison with KF93 and BM93, the GR93 scheme tends to produce more localized small-scale potential vorticity (PV) disturbances (Fig. 5a–c) over low troposphere and less diabatic heating/cooling over the high troposphere (Fig. 6b). The number of grid points with positive PV disturbances shows a high correlation (0.74) with that of TC intensity change (Fig. 6a), which implies that the energy of instability not consumed by convection may be available for the growth of TC intensity. Kuo et al. (1997) also

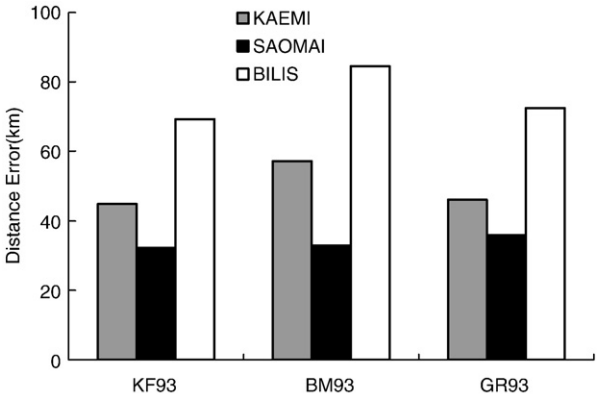

Fig. 7. Cases-averaged distance error (km/24 h) for each of the experiments.

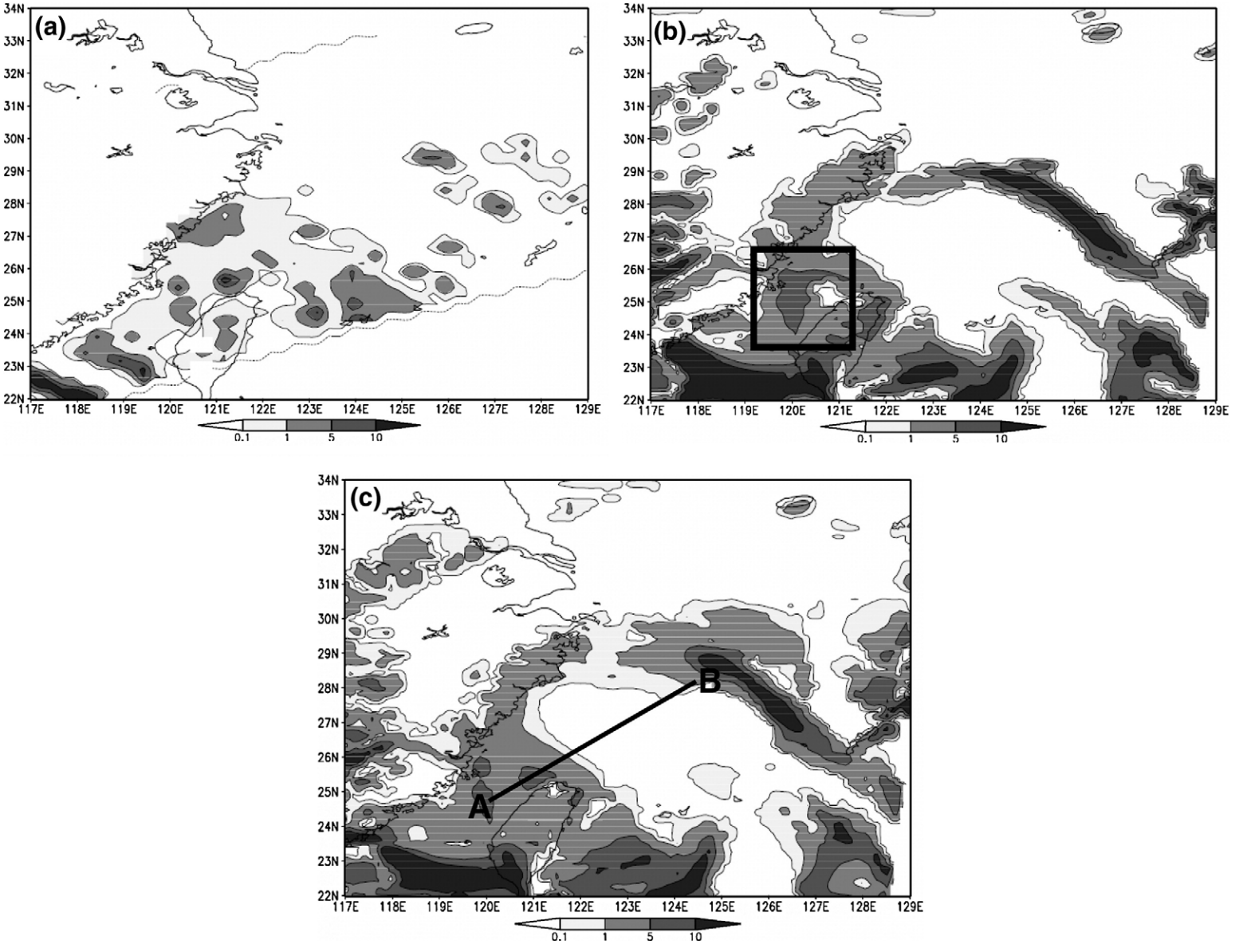

Fig. 8. Convective rainfall rate of observation and subgrid-scale rainfall simulation for Bilis at 1300 UTC Jul. 13, 2006. (a) TRMM/TMI convective rainfall rate (mm h^{-1}); (b) Subgrid-scale rainfall rate (mm h^{-1}) for KF93, and (c) as in (b), but for KFML. The rectangle in (b) shows the area of weak environmental flow. The thick solid line AB in (c) shows the location of cross section in Fig. 15.

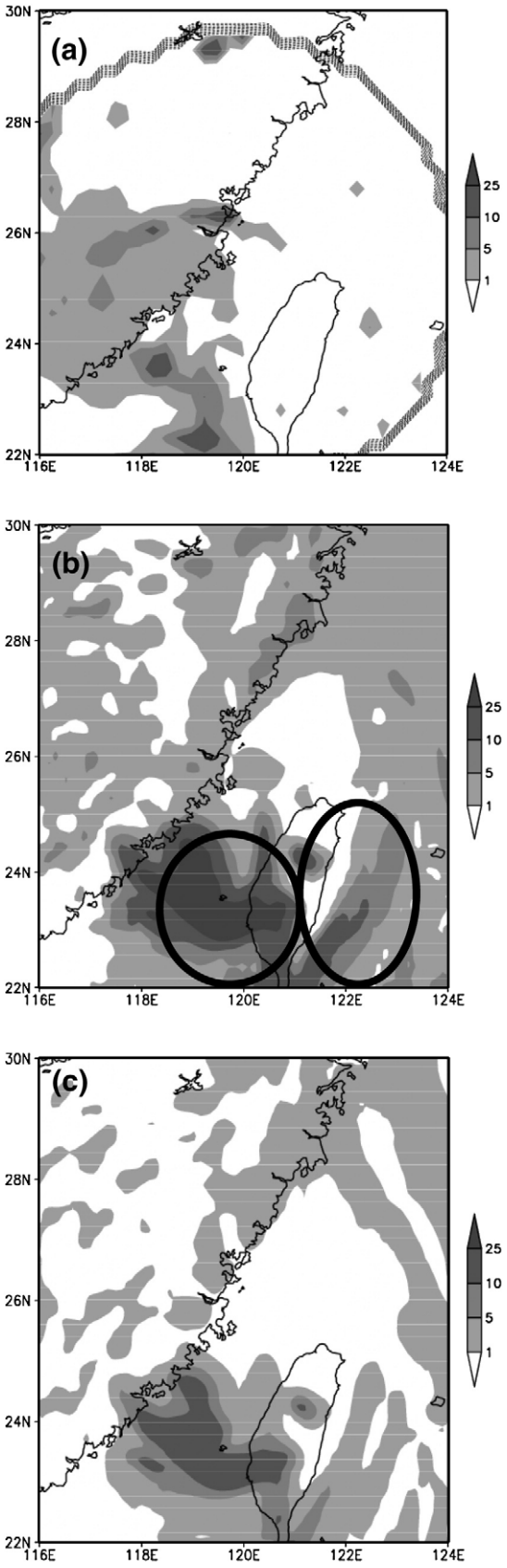

showed GR scheme tends to yield deep layers of absolute vertical instability characterized as saturated layers with a lapse rate considerably greater than moist adiabatic, which led to the development of intense localized circulations. For the track simulation, all the CPs perform satisfactorily (Fig. 7) with the 24 h maximum distance simulation error less than 100 km. In particular, KF93 produced the smallest track error of 50 km in 24 h, while BM93 made the largest error (70 km/24 h).

Our preliminary assessment of the performance of the CPs, based on the above verifications, is that the KF93 scheme can be used successfully in TC numerical modeling at the 15 km resolution used here.

4. Improvements on KF93

Despite the advantages shown above, KF93 can still be improved. A common criticism of the earlier version of the KF scheme was that it sometimes produced widespread light precipitation in marginally unstable environments (Warner and Hsu, 2000; Colle et al., 2003). This weakness is also identified in this study. Fig. 8 indicates that, within the Taiwan straits where large scale forcing is very weak due to the topography obstruction, the surface rainfall rate is overestimated by KF93, in comparison with the observations from TRMM/TMI. This deficiency of KF93 in weak environments may bear some relation to the parameterized convective triggering mechanism for its particular role in convection initialization (Kain, 2004), which deserves to be reexamined.

4.1. Original trigger function of KF93

KF93 estimates the instability available for cloud growth with a Lagrangian parcel method (Simpson and Wiggert, 1969). The first task in KF93 is to identify updraft source layers (USL) for parcels with a trigger function. Starting from the surface, vertically adjacent model layers are mixed until the depth of the mixture exceeds a threshold (i.e., 60 hPa). The thermodynamic characteristics of USL are determined along with the temperature of this parcel at its lifting condensation level (LCL). In making the decision of convective initiation, parcel temperature is firstly compared with its ambient temperature at the parcel LCL. However, prior to convection, the parcel is usually colder than its environment and are negatively buoyant. A temperature perturbation δT_{vv}, which was originally defined as a function of grid-resolved vertical motion given that convection tends to be favored by background vertical motion (Fritsch and Chappel, 1980), must be added to the parcel to drive it upward. δT_{vv} is defined as,

$$\delta T_{vv} = c_1 w_G^{1/3} \tag{3}$$

where c_1 is a unit number with dimensions °C $s^{1/3}$ $cm^{-1/3}$; and w_G the vertical velocity (cm s^{-1}) at the LCL.

Fig. 9. Convective rainfall rate of observation and subgrid-scale rainfall simulation for Kaemi at 0700 UTC Jul. 25, 2006. (a) TRMM/TMI convective rainfall rate (mm h^{-1}); (b) Subgrid-scale rainfall rate (mm h^{-1}) for KF93, and (c) as in (b), but for KFML.

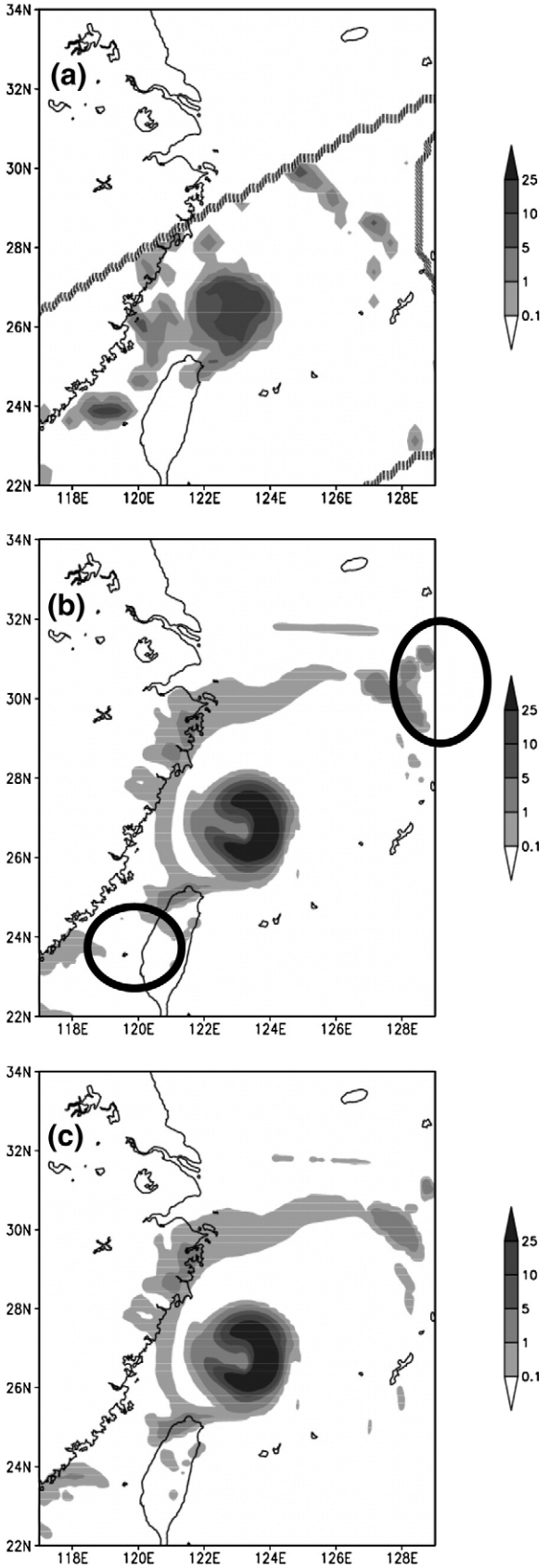

If the resultant parcel temperature is still less than the environmental value (i.e., $T_{LCL}+\delta T_{vv}<T_{ENV}$), then this parcel will be eliminated from consideration. The base of the USL is moved up one model level, and the above decision making process is repeated for a new potential USL. If, however, the perturbed parcel is warmer than its environment, it is ready for deep convection. Above the LCL, parcel vertical velocity is estimated at each model level using the Lagrangian parcel method, including the effects of entrainment, detrainment, and water loading (Frank and Cohen, 1987; Bechtold et al., 2001).

4.2. New definition on temperature perturbation

Obviously, the definition of δT_{vv} is very crucial in determining the prerequisite for a parcel to move upward and to trigger convection. The original assumption of temperature perturbation by vertical motion was given by Fritsch and Chappel (1980) based on the understanding of the role of convergence in destabilizing and moistening the atmosphere (Chen and Orville, 1980). Unfortunately, the effect of convergence in convection development has received much criticism (Arakawa, 2004; Emanuel, 1986). For instance, Arakawa (2004) emphasized the importance of moisture advection instead of convergence in determining the boundary layer specific humidity, which fuels convection.

It is noticed in this study that only in the area with plenty of moisture (Fig. 11c), the spatial temperature anomaly shows a close correlation with that of vertical motion in coverage and magnitude. Whereas in the area with depleted moisture, the correlation is negligible (Fig. 11a and b). This can be understood through a thermodynamic equation given below:

$$c_p\frac{dT}{dt}-\frac{ART}{p}\frac{dp}{dt}=Q-L\frac{dq}{dt} \tag{4}$$

where c_p is the specific heat at constant pressure, R the gas constant for dry air, L the latent heat of condensation, A the energy constant (0.23885 Cal/J). Other variables assume their usual meaning.

Note in Eq. (4) the rate of change of temperature change ($\frac{dT}{dt}$) is governed by $\frac{dq}{dt}$, which is determined by moisture advection as argued by Arakawa (2004).

To avoid the convergence controversy while introducing the effect of moisture advection, a new algorithm is proposed here to define the temperature perturbation. The total temperature perturbation is composed of horizontal (δT_{vvh}) and vertical (δT_{vvv}) components, with an accompanying weighting coefficient to represent the contribution of moisture advection.

Fig. 10. Convective rainfall rate of observation and subgrid-scale rainfall simulation for Saomai at 0000 UTC Aug. 10, 2006. (a) TRMM/TMI convective rainfall rate (mm h^{-1}); (b) Subgrid-scale rainfall rate (mm h^{-1}) for KF93, and (c) as in (b), but for KFML. The thick circles indicate the difference of simulation between KF93 and KFML.

The new algorithm is given by

$$\delta T_{vv} = R_h \cdot \delta T_{vvh} + R_v \cdot \delta T_{vvv} \quad (5)$$

where δT_{vvh} is the temperature spatial anomaly for each local grid point against the horizontal environmental temperature average (average over 9 closest grid points surrounding the target grid point), δT_{vvv} the temperature anomaly at LCL of each of the grid point against the vertical environmental temperature average (average of three sigma levels, i.e., LCL-1, LCL, LCL+1). R_h and R_v are the normalized horizontal and vertical moisture advections, respectively. The normalization algorithm is given below:

$$R_{h,v} = \frac{\vec{v}_M \cdot \nabla q_M - Min(\vec{v}_M \cdot \nabla q_M)_{h,v}}{Max(\vec{v}_M \cdot \nabla q_M)_{h,v} - Min(\vec{v}_M \cdot \nabla q_M)_{h,v}}. \quad (6)$$

where $\mathrm{Min}(\vec{v}_M \cdot \nabla q_M)_{h,v}$ and $\mathrm{Max}(\vec{v}_M \cdot \nabla q_M)_{h,v}$ are calculated within the same grid boxes as that of δT_{vvh} and δT_{vvv}.

Notice that both R_h and R_v are non-dimensional variables with the magnitude between 0 and 1. In each of the grid boxes, bigger (smaller) R_h or R_v is associated with stronger (weaker) moisture advection and temperature perturbation. The maximum magnitudes of R_h and R_v yield the maximum temperature perturbation (i.e., $\delta T_{vv} = \delta T_{vvh} + \delta T_{vvv}$).

This new algorithm explicitly establishes the positive relationship between grid scale temperature anomaly (represented by the effect of environmental forcing) and local forced convective disturbance.

4.3. Performance of the new trigger function

Performance of the original (KF93) and new trigger algorithm (hereafter KFML) are evaluated in sensitivity experiments.

4.3.1. Rainfall and track

The simulation of Bilis with KFML scheme shows consistency with the TRMM/TMI observation. It has reduced the area coverage of intense subgrid-scale rainfall (greater than 10 mm h^{-1}) generated by KF93 (Fig. 8). In particular, over the area of weak environmental forcing, the distribution as well as the intensity of subgrid-scale rainfall agrees well with that retrieved by TRMM/TMI. The improvement in the subgrid-scale rainfall simulation with KFML is also indicated in the simulations of Kaemi (Fig. 9) and Saomai (Fig. 10). Simulated rainfall regions most clearly affected by the modification of the algorithm are indicated by thick circles. It is seen that the new algorithm considerably reduces the subgrid-scale rainfall intensity over the moisture transportation channel (Fig. 11c), which has been overestimated in KF93. Fig. 12 shows the temporal evolution of the percentage of subgrid-scale rain simulated by KF93 and KFML. Note that KFML reduces the subgrid-scale rain by about 10%, irrespective of the different situations of the TC cases. Meanwhile for various TC cases, the simulated grid-scale rainfall by KFML shows negligible difference with that of KF93 (figure is not given).

Statistical verification for total rainfall (including subgrid-scale and grid-scale rainfall) accumulation is given in Fig. 13. It is noted that for light (i.e., less than 10 mm/24 h) and medium rainfall (i.e., greater than 10 mm/24 h), KFML increases the Threat Score by about 30% and 25%, respectively, in comparison with KF93 (Fig. 13a). Bias scores also give the consistent results (Fig. 13b), which indicate that KFML can reduce the overestimation indicated in KF93. Due to its more realistic depiction of convection, which interacts with and influences the large-scale environmental flow, KFML also reduces the track error by about 10% (Fig. 14). The tendency towards improvement is seen to increase with the time during the model integration.

4.3.2. Behavior in reducing instability

Fig. 15 shows the vertical structure of equivalent potential temperature and wind along the thick line AB shown in Fig. 8c, which illustrates an unstable situation under weak environmental forcing. The most unstable region prior to the time of observed convective rainfall is characterized by the warm tongue of equivalent temperature extending upward from the surface, accompanied by strong ascent transporting moisture and energy upward. Before and after the time of observed convective rainfall, the height (700 hPa) that the warm tongue of 365 K air reaches shows negligible change in KF93 (Fig. 15a and b). Whilst in the KFML experiment, the height that the 365 K isotherm extends descends from 700 hPa (Fig. 15a) to 900 hPa (Fig. 15c). Similar results can also be drawn from the *T*log*P* plot (Fig. 16), in which the CAPE energy calculated at the grid point with maximum observed convective rainfall is more efficiently consumed in the experiment KFML in comparison with that of KF93. In the KFML experiment the CAPE value is 1103 J kg^{-1} and 678 J kg^{-1} prior to and after the time of convective rainfall respectively, with nearly 38% energy being consumed. However in the KF93 experiment, the exhausted CAPE is only about 17%.

Meanwhile, for the marginally unstable area beside the warm tongue, the energy of instability is barely consumed by KFML, and is significantly less than that of KF93. This accounts for the overall reduction of subgrid rainfall.

4.3.3. Convective response to environmental humidity

The sensitivity of cumulus convection to humidity in the troposphere has been broadly recognized by pervious observational and modeling studies (i.e., Derbyshire et al., 2004; Raymond and Zeng, 2000). In this study the connection between humidity and convection has been reestablished through the new trigger algorithm with the consideration of moisture advection, which may affect this sensitivity. Fig. 17 shows the approximated linear relationship between domain-averaged relative humidity and latent heat flux in the low levels of the model (between 950 and 700 hPa) in the simulation of Bilis. The amount of latent heat flux represents the overall activity of boundary layer disturbance which favors the genesis of convection. In comparison with the original scheme, it is seen that the same amount of relative humidity is associated with reduced latent heat flux in the KFML experiment, which damps the activity of convection (Fig. 18a and b). The weakened convection then reduces the upward transportation of moisture from low troposphere (Fig. 18c and d), and accounts for the reduction in convective rainfall that is

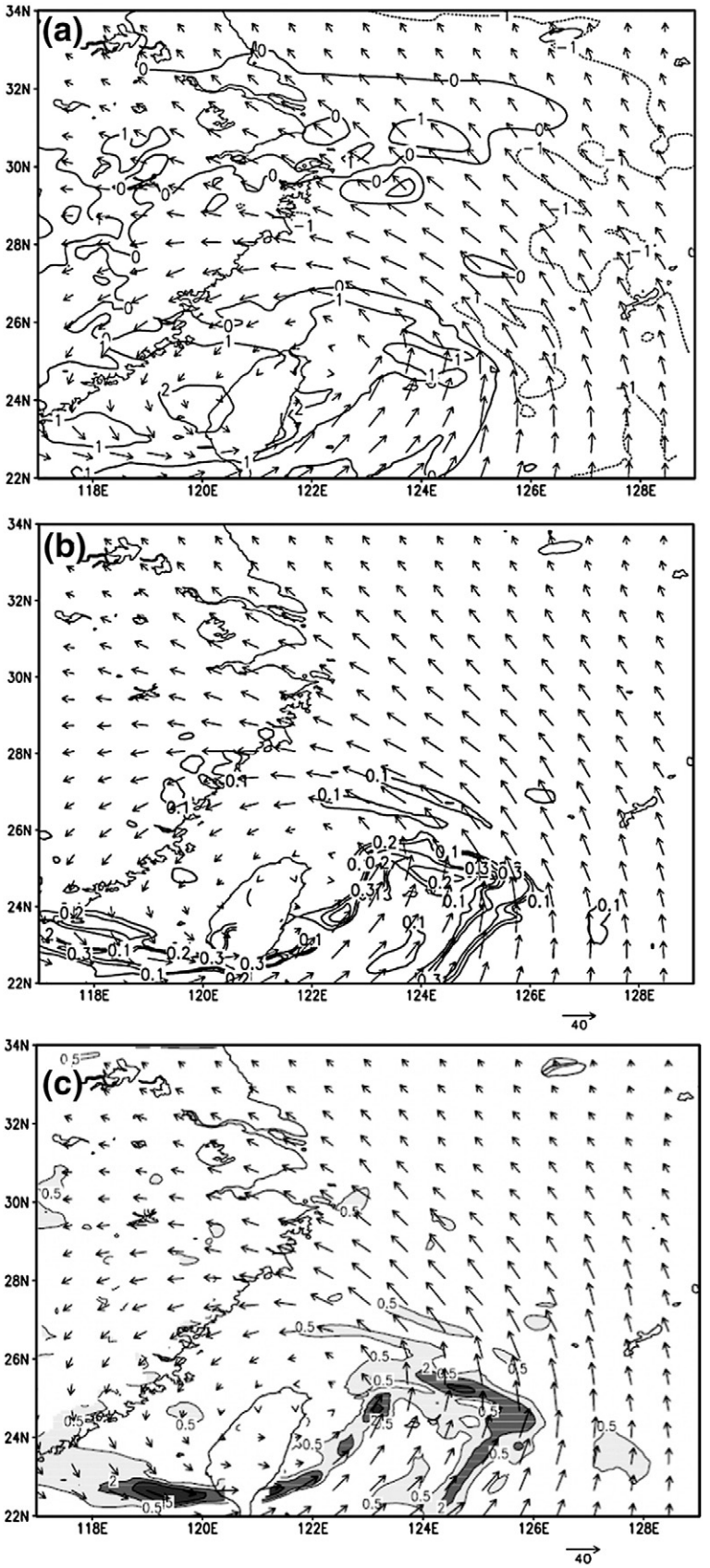
(a)
(b)
(c)
34N
32N
30N
28N
26N
24N
22N
118E
120E
122E
124E
126E
128E
40

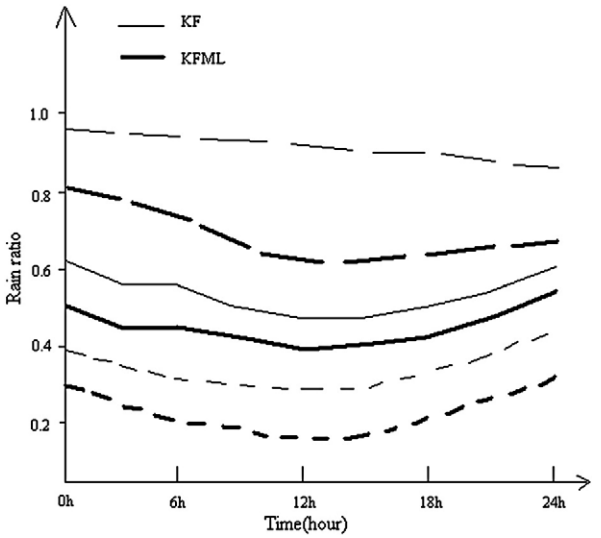

Fig. 12. Temporal evolution of the ratio of subgrid-scale rain in total rain simulated by experiment KF93 and KFML; solid line for Bilis (2006), short dashed line for Kaemi (2006), and long dashed line for Saomai (2006).

overestimated by the KF93 scheme. The reduction of latent heat flux due to the modification of the trigger algorithm is more evident in high relative humidity environments (Fig. 17). For example, for the moist environment with relative humidity of 88% and 92%, the reduction of latent heat flux is about 10 and 20 W m^{-2}, respectively.

5. Summary

The objective of this study is to improve the behavior of the CP in TC prediction. We evaluated three of the most popular CP schemes for simulation of TCs which made landfall on the east coast of China in 2006. Sensitivity experiments were designed with different CP schemes for simulation of TC rainfall, intensity and track. We have shown that the simulated intensity and coverage of TC rainfall, particularly its subgrid-scale component, is quite sensitive to different choices of CP scheme. In addition, for each of the CP scheme, the percentage of subgrid scale rainfall varies substantially for different TC cases, which implies that the behavior of the CP in rainfall simulations may be associated closely with specific characteristics of TC.

Moreover, it is shown that the GR93 scheme has a significant tendency to underestimate convective rainfall while still producing the most intense TC. Equipped with a sophisticated cloud algorithm, the KF93 scheme appears to be more accurate in simulations of rainfall, intensity and track, in comparison with GR93 and BM93.

However, despite its advantages, improvements to KF93 are still possible. For instance, the KF93 scheme has a considerable deficiency when large-scale signals or forcing are weak, as

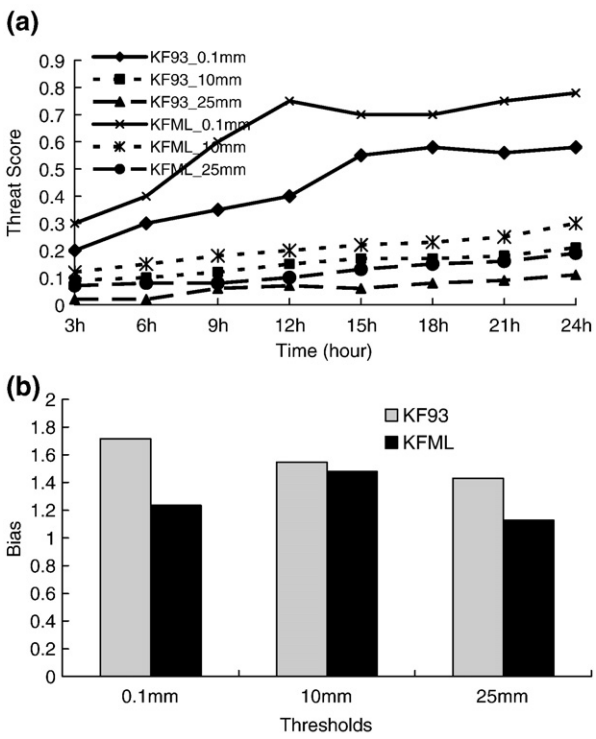

Fig. 13. (a) Threat Score for case-averaged 0–24 h rainfall simulation at 3-h intervals, and (b) Bias of case-averaged 24-h accumulated rainfall simulation in experiments KF93 and KFML at the thresholds of 0.1 mm/24 h, 10 mm/24 h and 25 mm/24 h.

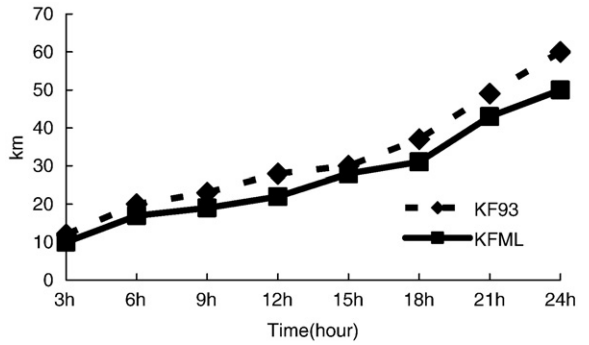

Fig. 14. Variation of the case-averaged 0–24 h distance simulation error for the two schemes (KF93 and KFML) at 3-h intervals.

identified in this study. The authors assume that this deficiency may bear a close relation to the original trigger function of KF93 for its particular role in convection initiation. In particular, the statistical relation between convective temperature perturbation and convergence-determined grid-scale vertical motion is theoretically not quite robust. To avoid this convergence-related controversy, a new formula is proposed in this study to redefine the convective temperature perturbation, in which the

Fig. 11. (a) 850 hPa wind vectors and vertical velocity (solid lines, m s^{-1}) for KF93 at 1300 UTC Jul. 13, 2006; (b) as in (a), but for temperature anomaly (solid lines, K) against the domain average; (c) as in (a), but for moisture convergence flux (shaded).

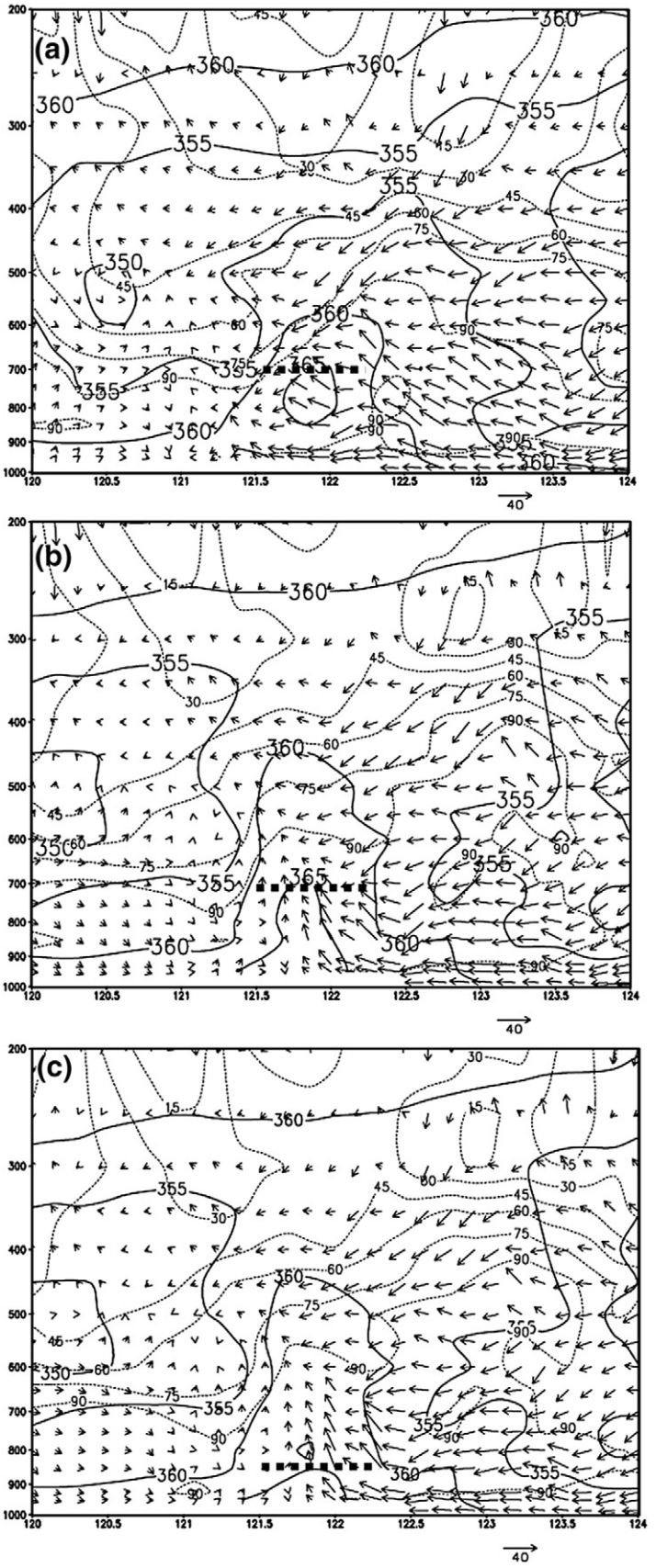
(a)
(b)
(c)
200
300
400
500
600
700
800
900
1000
120
120.5
121
121.5
122
122.5
123
123.5
124
40

particular role of moisture advection is taken into account. In this new algorithm, the relationship between environmental forcing (e.g., grid-scale temperature anomaly due to moisture and temperature advection) and local disturbance is explicitly established.

Preliminary experiments were conducted to verify this new algorithm. It has shown that the distribution as well as the intensity of convective rainfall was significantly improved with the new algorithm. The new algorithm also contributes to the improvement of TC track simulation (about 10%).

The new trigger scheme can reasonably eliminate convective instability under weak synoptic forcing. The response of the disturbance in the low troposphere to environmental humidity changes towards more realistic values.

This study has provided convincing evidence of the advantages of the new trigger algorithm. However, detailed examination is still required to extend the understanding of the physics behind the scheme.

Acknowledgements

This work was jointly supported by the National Natural Science Foundation of China under Grant 40705024, the Public Welfare Project sponsored by the Ministry of Science and Technology of China under Grant No. 2005DIB3J104 and Key project No. 06DZ12011 sponsored by Science and Technology Commission of Shanghai Municipality.

References

Alapaty, K., Madala, R.V., Raman, S., 1994. Numerical simulation of orographic convective rainfall with Kuo and Betts–Miller cumulus parameterization schemes. J. Meteorol. Soc. Japan 72, 123–137.

Anthes, R.A., 1977. A cumulus parameterization scheme utilizing a one-dimensional cloud model. Mon. Weather Rev. 105, 270–286.

Arakawa, A., 2004. The Cumulus parameterization problem: past, present, and future. J. Climate 13, 2493–2525.

Arakawa, A., Schubert, W.H., 1974. Interaction of a cumulus cloud ensemble with the large-scale environment, part I. J. Atmos. Sci. 31, 674–701.

Bechtold, P., Bazile, E., Guichard, F., Mascart, P., Richard, E., 2001. A mass-flux convection scheme for regional and global models. Q J. R. Meteorol. Soc. 127, 869–886.

Betts, A.K., 1986. A new convective adjustment scheme. Part I: observational and theoretical basis. Q. J. R. Meteorol. Soc. 112, 677–691.

Betts, A.K., Miller, M.J., 1993. The Betts–Miller scheme. In: Emanuel, K.A., Raymond, D.J. (Eds.), The Representation of Cumulus Convection in Numerical Models. Amer. Meteor. Soc. 246 pp.

Ceselski, B.F., 1974. Cumulus convection in weak and strong tropical disturbance. J. Atmos. Sci. 31, 1241–1255.

Charney, J.G., Eliassen, A., 1964. On the growth of the hurricane depression. J. Atmos. Sci. 21, 68–75.

Chen, C.-H., Orville, H.D., 1980. Effects of mesoscale convergence on cloud convection. J. Appl. Meteor. 19, 256–274.

Cohen, C., 2002. A comparison of cumulus parameterizations in idealized sea breeze simulations. Mon. Weather Rev. 130, 2554–2571.

Colle, B.A., Olson, J.B., Tongue, J.S., 2003. Multiseason verification of the MM5. Part II: Evaluation of High-resolution precipitation forecasts over the northeastern United States. Weather Forecasting 18, 458–480.

Derbyshire, S.H., Beau, I., Bechtold, P., Grandpeix, J.-Y., Piriou, J.-M., Redelsperger, J.-L., Soares, P.M.M., 2004. Sensitivity of moist convection to environmental humidity. Q. J. R. Meteorol. Soc. 130, 3055–3079.

Donner, L.J., 1993. A cumulus parameterization including mass fluxes, vertical momentum dynamics, and mesoscale effects. J. Atmos. Sci. 50, 889–906.

Dudhia, J., 1989. A nonhydrostatic version of the Penn State-NCAR mesoscale model. Mon. Weather Rev. 121, 1493–1513.

Emanuel, K.A., 1986. An air–sea interaction theory for tropical cyclones. Part I: steady-state maintenance. J. Atmos. Sci. 43, 585–604.

Emanuel, K.A., 1991. A scheme for representing cumulus convection in large-scale models. J. Atmos. Sci. 48, 2313–2335.

Frank, W.M., Cohen, C., 1987. Simulation of tropical convective systems. Part I: a cumulus parameterization. J. Atmos. Sci. 44, 3787–3799.

Fritsch, J.M., Chappel, C.F., 1980. Numerical prediction of convectively driven mesoscale pressure systems. Part I: convective parameterization. J. Atmos. Sci. 37, 1722–1733.

Gochis, D.J., Shuttleworth, W.J., Yang, Z., 2002. Sensitivity of the modeled North American monsoon regional climate to convective parameterization. Mon. Weather Rev. 130, 1282–1298.

Grell, G., 1993. Prognostic evaluation of assumptions used by cumulus parameterization. Mon. Weather Rev. 121, 764–787.

Grell, G., Dudhia, J. and Stauffer, D. 1994: A Description of the Fifth-Generation Penn State/NCAR Mesoscale Model (MM5). NCAR/TN-398 + STR.

Hogan, T.F., Pauley, R.L., 2007. The impact of convective momentum transport on tropical cyclone track forecasts using the Emanuel cumulus parameterization. Mon. Weather Rev. 135, 1195–1207.

Hong, S.-Y., Pan, H.-L., 1996. Nonlocal boundary layer vertical diffusion in a medium-range forecast model. Mon. Weather Rev. 124, 2322–2339.

Kain, J.S., 2004. The Kain–Fritsch convective parameterization: an update. J. Appl. Meteorol. 43, 170–181.

Kain, J.S., Fritsch, J.M., 1990. A one-dimensional entraining/detraining plume model and its application in convective parameterization. J. Atmos. Sci. 47, 2784–2802.

Kain, J.S., Fritsch, J.M., 1993. Convective parameterization for mesoscale models: the Kain–Fritsch scheme. The Representation of Cumulus Convection in Numerical Models, Meteor. Monogr., No. 46. Amer. Meteor. Soc., pp. 165–170.

Kummerow, C.D., Barnes, W., Kozu, T., Shiue, J., Simpson, J., 1998. The Tropical Rainfall Measuring Mission (TRMM) sensor package. J. Atmos. Ocean. Technol. 15, 809–817.

Kuo, H.L., 1974. Further studies of the parameterization of the influence of cumulus convection on large-scale flow. J. Atmos. Sci 31, 1232–1240.

Kuo, Y.-H., Reed, R.J., Liu, Y.-B., 1996. The ERICA IOP 5 storm. Part III: mesoscale cyclogenesis and precipitation parameterization. Mon. Weather Rev. 124, 1409–1434.

Kuo, Y.-H., Bresch, J.F., Cheng, M.D., Kain, J., Parsons, D.B., Tao, W.K., Zhang, D.L., 1997. Summary of a mini workshop on cumulus parameterization for mesoscale models. Bull. Am. Meteorol. Soc. 78, 475–491.

Li, Y., Yu, R., Fu, Y., Ye, C., 2008. A case study on triggering of thermal convective precipitation. Acta Meteorol. Sin. 66, 190–202 (in Chinese).

Liu, Y., Zhang, D.-L., Yau, M.K., 1997. A multiscale numerical study of Hurricane Andrew (1992). Part I: an explicit simulation. Mon. Weather Rev. 125, 3073–3093.

Ma, L.-M., Duan, Y., Zhu, Y., 2004. The structure and rainfall features of tropical cyclone Rammasun (2002). Adv. Atmos. Sci. 21, 951–963.

Ma, L.-M., Qin, Z., Duan, Y., Liang, X., Wang, D., 2006. Impacts of TRMM SRR assimilation on the numerical prediction of tropical cyclone. Acta Oceanol. Sin. 25, 14–26.

Ma, L.-M., Chan, J.C.L., Davidson, N.E., Turk, J., 2007. Initialization with diabatic heating from satellite-derived rainfall. Atmos. Res. 85, 148–158.

Mapes, B.E., 2004. Sensitivities of cumulus-ensemble rainfall in a cloud-resolving model with parameterized large-scale dynamics. J. Atmos. Sci. 61, 2308–2317.

Nagarajan, B., Yau, M.K., Zhang, D.-L., 2001. A numerical study of a mesoscale convective system during TOGA COARE. Part I: model description and verification. Mon. Weather Rev. 129, 2501–2520.

Nasuno, T., Tomita, H., Iga, S., Miura, H., Satoh, M., 2007. Multiscale organization of convection simulated with explicit cloud processes on an aquaplanet. J. Atmos. Sci. 64, 1902–1921.

Ooyama, K., 1964. A dynamical model for the study of tropical cyclone development. Geofis. Int. 4, 187–198.

Ooyama, K., 1971. A theory on parameterization of cumulus convection. J. Meteorol. Soc. Japan 49, 744–756.

Puri, K., Miller, M.J., 1990. The use of satellite data in the specification of convective heating for diabatic initialization and moisture adjustment in numerical weather prediction models. Mon. Weather Rev. 118, 67–93.

Raymond, D.J., Zeng, X., 2000. Instability and large-scale circulations in a two-column model of the tropical troposphere. Q. J. R. Meteorol. Soc. 126, 3117–3135.

Fig. 15. (a) Vertical cross section of equivalent potential temperature, relative humidity and wind vector in KF93 at 1200 UTC Jul. 13, 2006 along the thick solid line AB indicated in Fig. 8c, (b) as in (a), but for 1400 UTC Jul. 13, 2006, and (c) as in (b), but for experiment KFML. The thick dashed lines indicate the height that the warm tongue of 365 K air reaches.

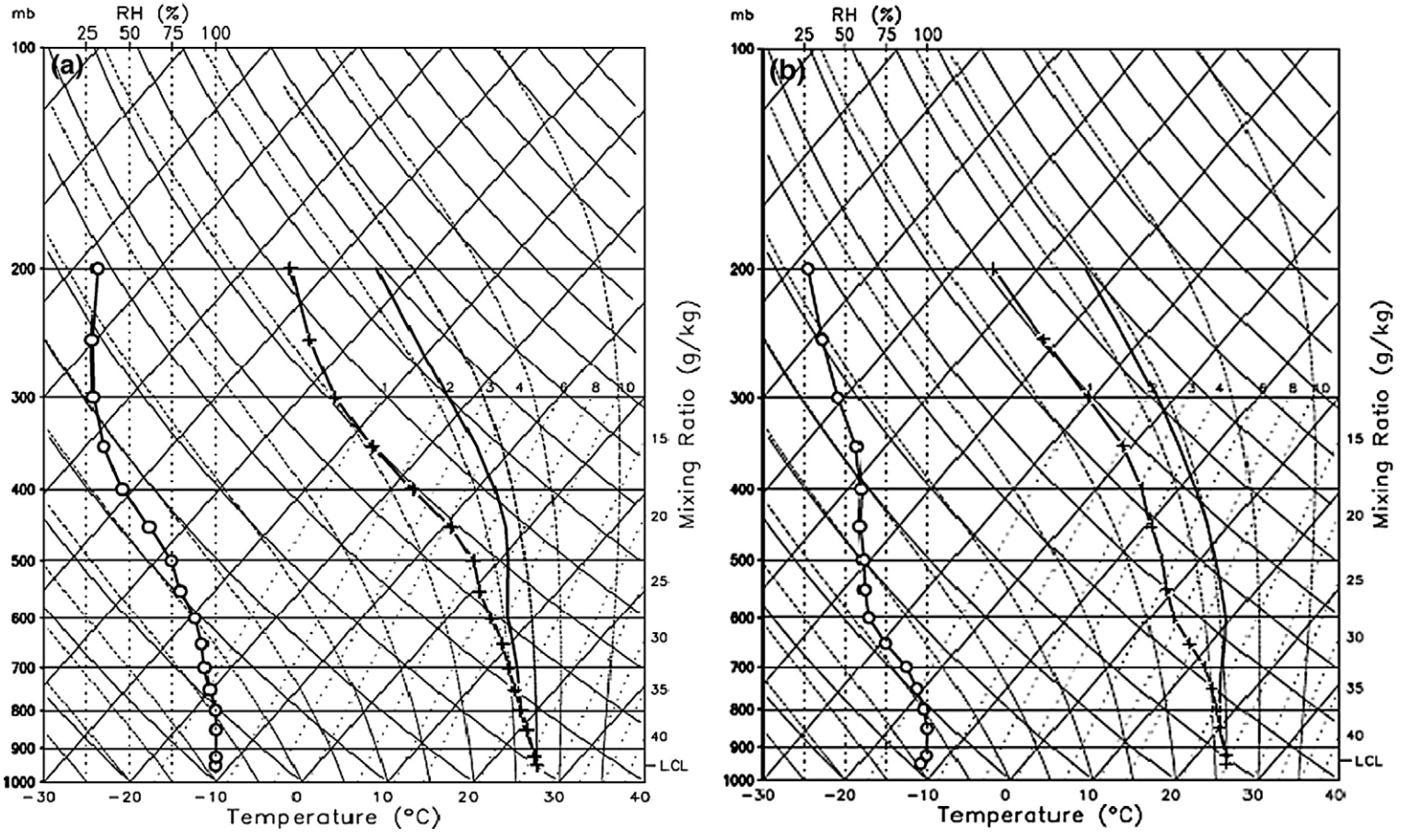

Fig. 16. (a) *T*log*P* plots in KF93 at the grid point closest to the observed maximum rainfall rate in Fig. 8a at 1200 UTC Jul. 13, 2006; (b) as in (a), but for 1400 UTC Jul. 13, 2006; (c) as in (b), but for KFML. The curves with crosses and squares indicate environmental temperature and relative humidity respectively, while the thick curve indicates the dew point.

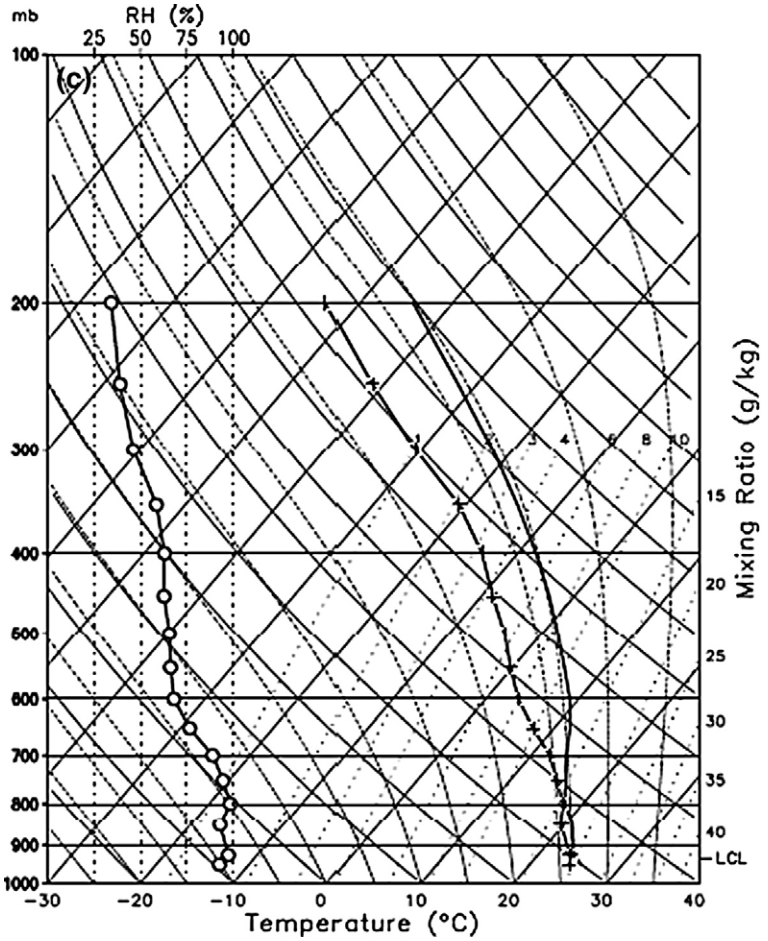

Fig. 16 (*continued*).

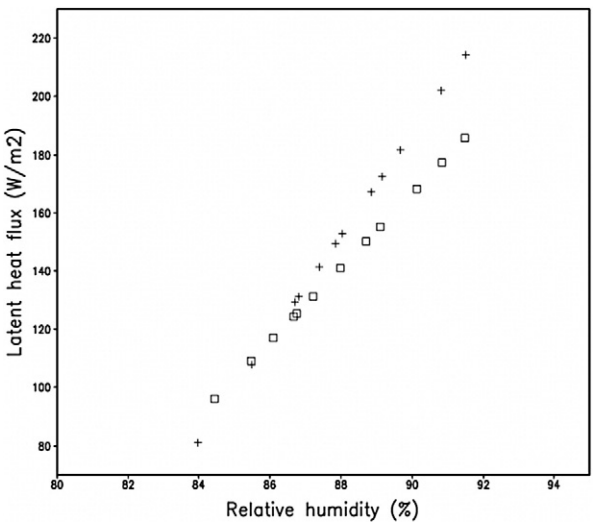

Fig. 17. Approximated linear relationship between domain-averaged surface latent heat flux and relative humidity for the simulation of Bilis. Solid and dashed lines indicate the results of KFML and KF93, respectively.

Simpson, J., Wiggert, V., 1969. Models of precipitating cumulus towers. Mon. Weather Rev. 97, 471–489.
Tiedtke, M., 1989. A comprehensive mass flux scheme for cumulus parameterization in large-scale models. Mon. Weather Rev. 117, 1779–1800.
Wang, W., Seaman, N.L., 1997. A comparison study of convective parameterization schemes in a mesoscale model. Mon. Weather Rev. 125, 252–278.
Warner, T.T., Hsu, H.M., 2000. Nested-model simulation of moist convection: The impact of coarse-grid parameterized convection on fine-grid resolved convection through lateral-boundary-condition effects. Mon. Weather Rev. 128, 2211–2231.
Weisman, M.L., Skamarock, W.C., Klemp, J.B., 1997. Resolution dependence of explicitly modeled convective system. Mon. Weather Rev. 125, 527–548.
Xiao, Q., Zou, X., Wang, B., 2000. Initialization and simulation of a landfalling hurricane using a variational bogus data assimilation scheme. Mon. Weather Rev. 128, 2252–2269.
Yang, M.-J., Tung, Q.-C., 2003. Evaluation of rainfall forecasts over Taiwan by four cumulus parameterization schemes. J. Meteorol. Soc. Japan 81, 1163–1183.
Zhu, T., Zhang, D.-L., 2006. Numerical simulation of Hurricane Bonnie (1998). Part II: sensitivity to varying cloud microphysical processes. J. Atmos. Sci. 63, 109–126.
Zou, X., Xiao, Q., 2000. Studies on the initialization and simulation of a mature hurricane using a variational bogus data assimilation scheme. J. Atmos. Sci. 57, 836–860.
Zou, X., Vandenberghe, F., Pondeca, M., Kuo, Y.-H., 1997. Introduction to adjoint techniques and the MM5 adjoint modeling system. NCAR Technical Note, NCAR/TN-435+STR.

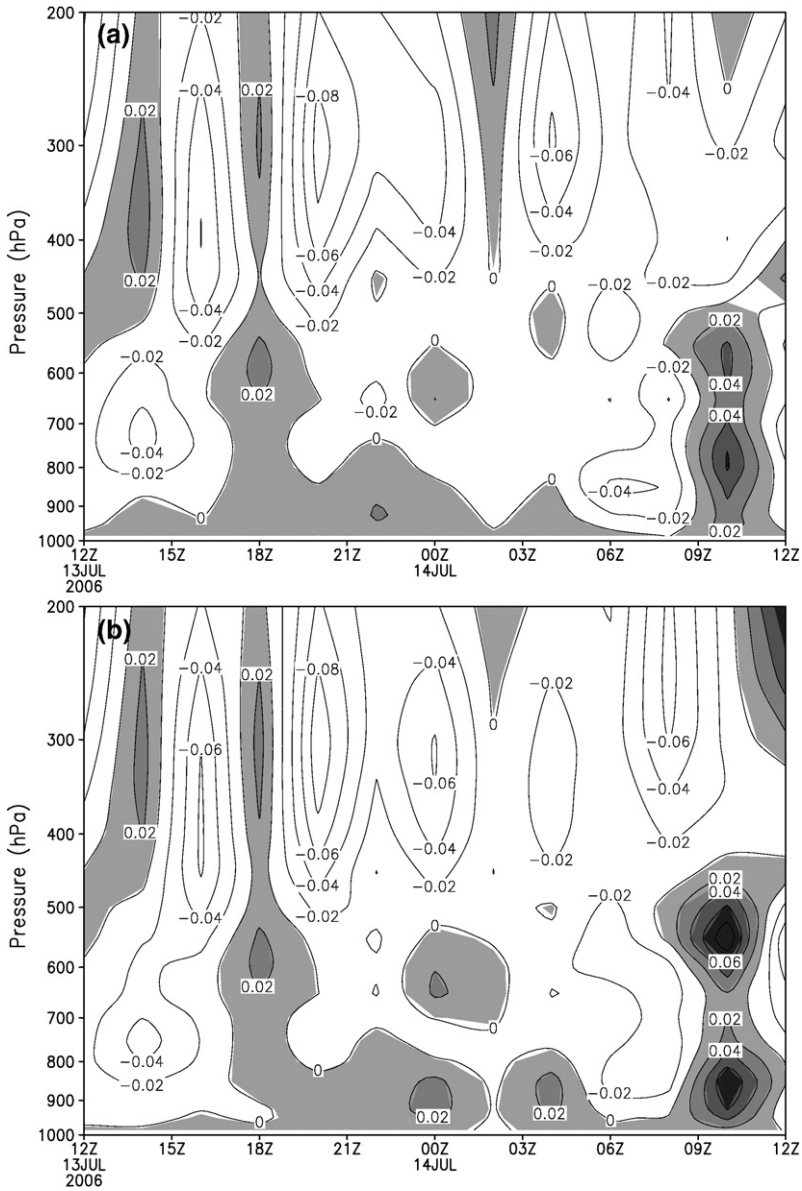

Fig. 18. Temporal evolution of the domain-averaged vertical velocity (m s^{-1}) (a: KFML, b: KF93) and relative humidity (c: KFML, d: KF93) generated by KFML and KF93 during 12 UTC 13 July–12 UTC 14 July, 2006 over the convective unstable area indicated by the rectangle in Fig. 8b.

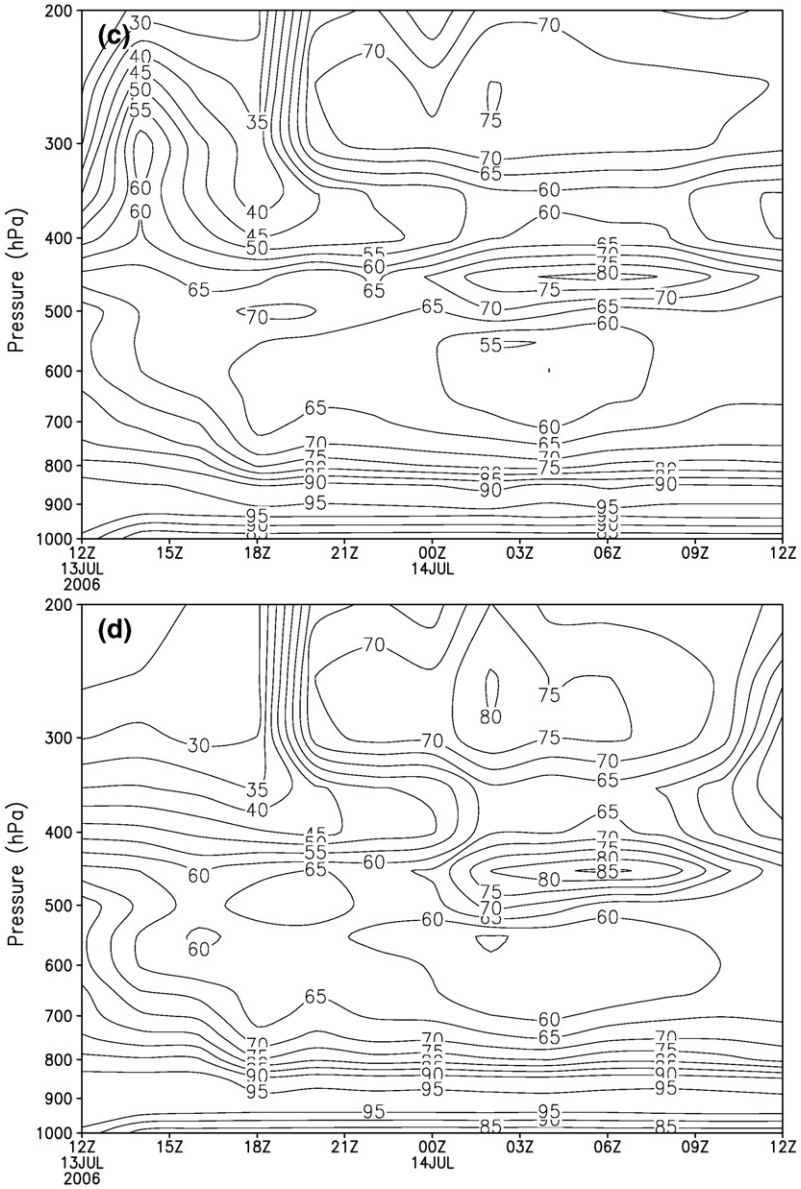

Fig. 18 (*continued*).